Journal of Hydroinformatics

Journal of Hydroinformatics Vol 24 No 2, 333 doi: 10.2166/hydro.2021.087

Evaluation of hydrodynamic behavior of biosand filters using computational fluid dynamics combined with the design of experiments

Dominique Martins Sala [a], Ricardo Vicente de Paula Rezende [b] and Sandro Rogério Lautenschlager [a,*]

[a] Department of Civil Engineering, State University of Maringá, Maringá, PR 87020-900, Brazil
[b] Department of Chemical Engineering, State University of Maringá, Maringá, PR 87020-900, Brazil
*Corresponding author. E-mail: srlager@uem.br

DMS, 0000-0002-1741-1952; RV de PR, 0000-0001-8349-9705; SRL, 0000-0003-3219-2257

ABSTRACT

Biosand filters (BSFs) are widely used in rural and urban areas where access to drinking water is limited or non-existent. This study applies computational fluid dynamics in the assessment of hydrodynamic characteristics considering changes in the design of two BSF models to make construction options available to communities, without losing hydrodynamic efficiency. The commercial code ANSYS-CFX 20.1 together with a central composite design of experiments methodology to simulate the flow was used under different combinations of porosities, permeabilities, pipe diameters, and filter diameters and heights. These parameters were combined statistically from Statistica 13.3. Our results have shown that combining greater filter depths with smaller pipe diameters has played a key role in the BSF best performance, and the CAWST V10 model has performed better than HydrAid, with lower velocities and longer hydraulic retention times.

Key words: ANOVA, biosand filter, design of experiments, CFD, point-of-use water treatment technologies, porous media flow

HIGHLIGHTS

- Stable mathematical models predict water flow patterns in biosand filters.
- The CAWST V10 model promoted more favorable hydrodynamic conditions for microbiological treatment than HydrAid.
- The performance in water treatment is obtained for different heights and diameters of filters, and different diameters of tubes.

GRAPHICAL ABSTRACT

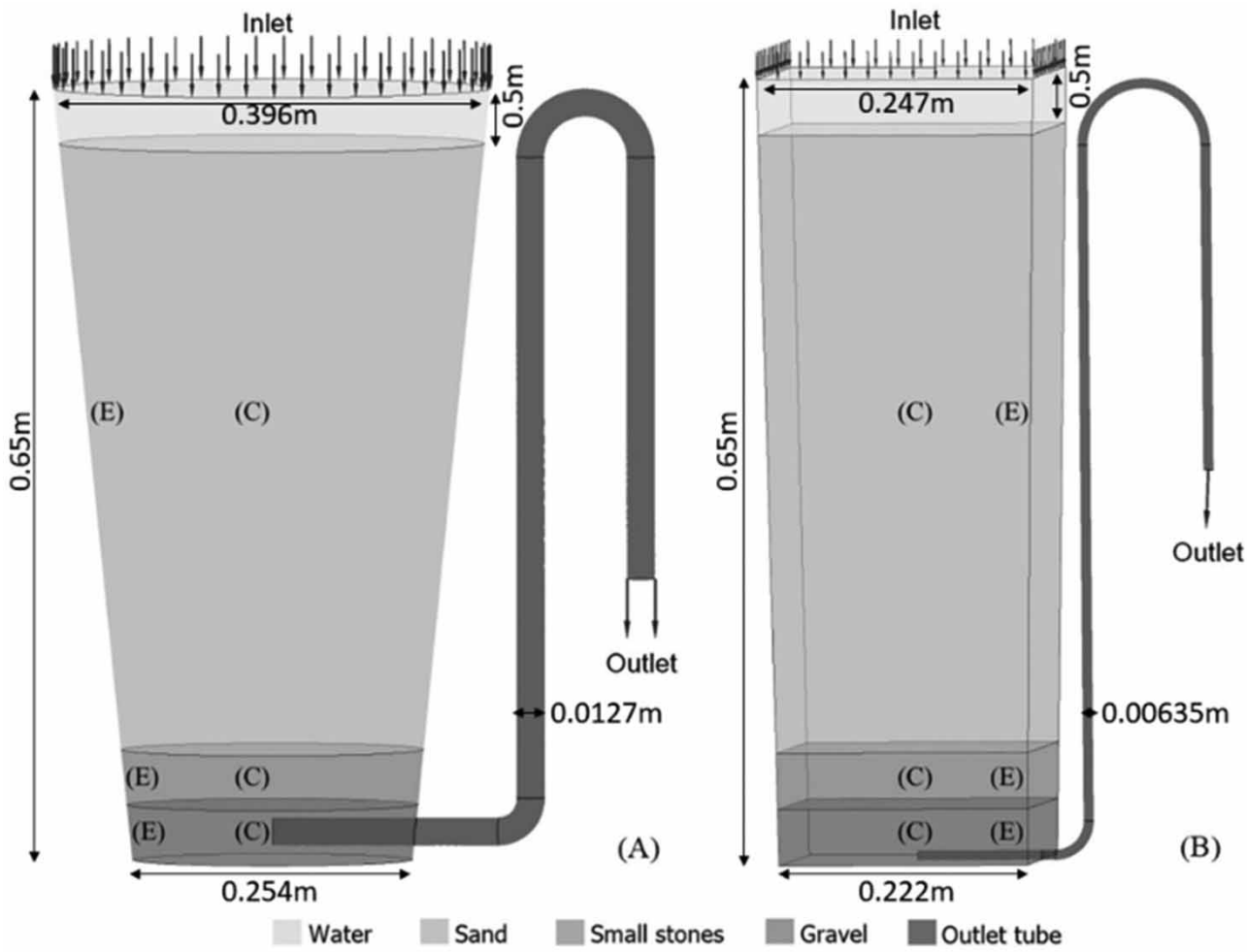

1. INTRODUCTION

Point-of-use (POU) water treatment technologies combine physical and biological treatments (Chawla *et al.* 2017) in a smart and cheap solution to rural and urban areas where access to drinking water is limited or nonexistent (Kennedy *et al.* 2012); that is, it is an accessible and easy to implement technology. One of the most promising POU technologies is the biosand filter (BSF), distributed worldwide by nonprofit organizations (Chan *et al.* 2018).

According to Singer *et al.* (2017), at the top of the BSF, there is a biological degradation of organic matter, precisely in the *schmutzdecke* (a biofilm layer), and this process extends to the sand layer due to the limited availability of oxygen and nutrients reaching efficiencies of 98% for *E. coli* removal; 96.25% for total coliforms; and 94.8% for turbidity (Chan *et al.* 2018; Sizirici 2018). However, this performance is heavily influenced by the hydrodynamic behavior in the BSF. This was investigated by Qi *et al.* (2013), varying the types of tubes and diameters of the filter media.

With characteristic surface velocities ranging from 4 to 40 cm h^{-1} (Carpenter & Helbling 2017), it can be observed that in low-velocity areas, the development of biofilms is favored; and conversely, in high-velocity zones, there is a decrease in the biofilm due to shorter contact times with microbial communities and higher hydrodynamic shear forces, affecting substrate biotransformation. In addition, with very low velocities, there is a greater probability of porous clogging due to biofilm encrustation (Ait-Mouheb *et al.* 2019).

Computational fluid dynamics (CFD) has been a widely used tool to study and optimize water treatment operations (Karpinska *et al.* 2015). It is economically advantageous (Vilà-rovira *et al.* 2017) and allows the reduction of experimental

efforts (Nørregaard *et al.* 2019). In Mesquita *et al.* (2012), commercial sand filters were evaluated for different sizes of sand particles and layer depths. Berbert *et al.* (2016) studied the hydrodynamics of two models of commercial filters (HydrAid and CAWST V10) by CFD and found that the intake tube design changes the flow streamlines path and the size of the dead zones. However, simulations of BSFs using CFDs are still scarce, especially in small filters (Chen *et al.* 2019). More detailed studies are needed to provide communities with construction and use options without losing hydrodynamic efficiency in treatment.

Thus, from the original design of two commercial filters (HydrAid and CAWST V10), this study aims to model and to describe how the flow is affected by changes in filter geometry, as well as filter media parameters such as strength and permeabilities, and thus determine the key factors for better filter operation. No mass transfer, or the *schmutzdecke* grow, or transport of chemical compounds are considered.

The proposed model was solved through CFD techniques associated with a design of experiment (DoE) by applying a central composite design (CCD) for the combination of analysis factors. The data are then subjected to statistical ANOVA and response surface methodology (RSM).

2. MATERIAL AND METHODS

2.1. Mathematical approach

All assumptions that support the mathematical model are listed below:

- steady-state one-phase laminar flow;
- incompressible fluid and isothermal one-phase flow at 25 °C (water);
- each layer of porous media has a local constant porosity and permeability chosen as a representative average value of the entire layer;
- normal and uniform inlet velocity;
- average static outlet pressure set to 0.0 Pa; and
- density (997 kg m^{-3}) and dynamic viscosity (8,899 $\times$ 10^{-4} kg m^{-1} s^{-1}) remain constant (Bagheri & Mohseni 2014).

The one-phase approach allows running several cases with no prohibitive computational times associated with unsteady free-surface two-phase flows. Furthermore, it is not necessary to account for any buoyancy.

2.1.1. Governing equations

The mass and momentum mathematical model for porous media models is a volume average formulation of the Navier–Stokes. The porosity of the media is defined as the ratio between the available volume V' and the total volume (Rezende *et al.* 2010; ANSYS 2020):

$$\varepsilon = \frac{V'}{V}, \tag{1}$$

therefore, the area available for the flow is

$$\vec{A'} = \overline{\overline{K}} \cdot \vec{A}, \tag{2}$$

where $\overline{\overline{K}}$ is the porosity tensor, which in turn is considered a second-order symmetric tensor, $K_{ij} = \varepsilon\delta_{ij}$.

Considering an incompressible flow assumption, mass conservation becomes

$$\vec{\nabla} \cdot (\rho\overline{\overline{K}} \cdot \vec{U}) = 0, \tag{3}$$

being ε the porosity of biofilter media and ρ is the fluid density. The momentum equation is given by the following equation:

$$\frac{\partial}{\partial t}(\varepsilon\rho\vec{U}) + \vec{\nabla} \cdot [(\rho(\overline{\overline{K}} \cdot \vec{U}) \otimes \vec{U}] - \vec{\nabla} \cdot (\mu\overline{\overline{K}} \cdot (\nabla\vec{U} + \nabla\vec{U}^T) = \varepsilon\vec{S}^M - \varepsilon\vec{\nabla}\rho\,. \tag{4}$$

Here, $\vec{U}$ is the volume-averaged velocity. The momentum source term originated in the averaging process is given as follows:

$$\varepsilon \vec{S}^{M} \equiv -\bar{\bar{R}} \cdot \vec{U}, \tag{5}$$

where $\bar{\bar{R}}$ represents the mean resistance tensor. At the limit, when the resistance to flow is high, that is, $\vec{U}$ tends to be zero, the right side of Equation (4) becomes larger than the left side, hence

$$\vec{U} \cong (-\bar{\bar{R}}^{-1}) \cdot \nabla \rho, \tag{6}$$

which is the anisotropic formulation of Darcy's law. Neglecting inertial losses due to the low velocity of the problem, for a homogeneous and isotropic media, we have:

$$\vec{S}^{M} = -\frac{\mu}{K_{\text{perm}}} \vec{U}. \tag{7}$$

Hojo *et al.* (2022) and Berbert *et al.* (2016) have employed this approach to analyze these commercial filters and validated by the residence time distribution technique.

2.2. Numerical method

ANSYS-CFX R20.1 was used to solve the mathematical model. The pressure–velocity coupling method is a fourth-order Rhie–Chow (Martínez *et al.* 2017). A high-resolution differentiation scheme was applied (Almeida *et al.* 2020), and the time derivative has a second backward Euler formulation. The convergence criterion was a root-mean-square residual of $<10^{-6}$ performed with double precision. The average wall clock time was next to 9 min per run in a 2.90 GHz Intel® Core™ i7-7500 U processor with an 8 GB of RAM.

2.3. Geometry

All geometric regions and the porous media layers are indicated and named in Figure 1 to clarify their association with physics and respective boundary conditions.

To verify the impact of geometric changes in the original designs, for a second part of the experiments, variations in the filter's height and diameter and the outlet tube's diameter of the outlet tube have been done. The criteria for choosing the dimensions studied were based on the usability and ease of finding materials with the same proportions in the country of study (Brazil). The values studied for the diameter of the outlet tube were 0.0127 ($d1$), 0.03175 ($d2$), and 0.0508 ($d3$). All parameter values are shown in Table 1.

2.4. Meshing

In both cases (H and CW filters), an unstructured mesh composed of tetrahedral elements for the core of the flow was employed. The minimum size of the mesh element was 0.007 m in the filter region with boundary inflation of five layers, which were generated in the regions next to the wall tubes, inside the filter. The outlet tubes also contain four-layer wall inflation, and these inflation layers were added to capture the profile of the boundary layer and avoid numerical instabilities due to possible abrupt changes in pressure and velocity, as well as the changes in the physical properties between domains.

The generated mesh for HydrAid has 2.3 million nodes and 1.6 million elements, and for CAWST V10, 2.0 million nodes and 1.3 million elements considered the velocities magnitudes involved in this kind of flow – usually very slow – they can be considered fine meshes. As the ANSYS-CFX uses a cell-vertex finite volume formulation, the number of finite volumes and, consequently, the size of the linear system is defined by the number of nodes instead of the number of elements.

A mesh independence study was performed and more details regarding the mesh parameters are given in the Supplementary Appendix.

2.5. Boundary conditions

In the actual BSF operation, there are two ways to operate it: an intermittent feed, with some batch, or a continuous feed. In the first, one has a variable water column, and the hydraulic head will change along the time changing the superficial velocity

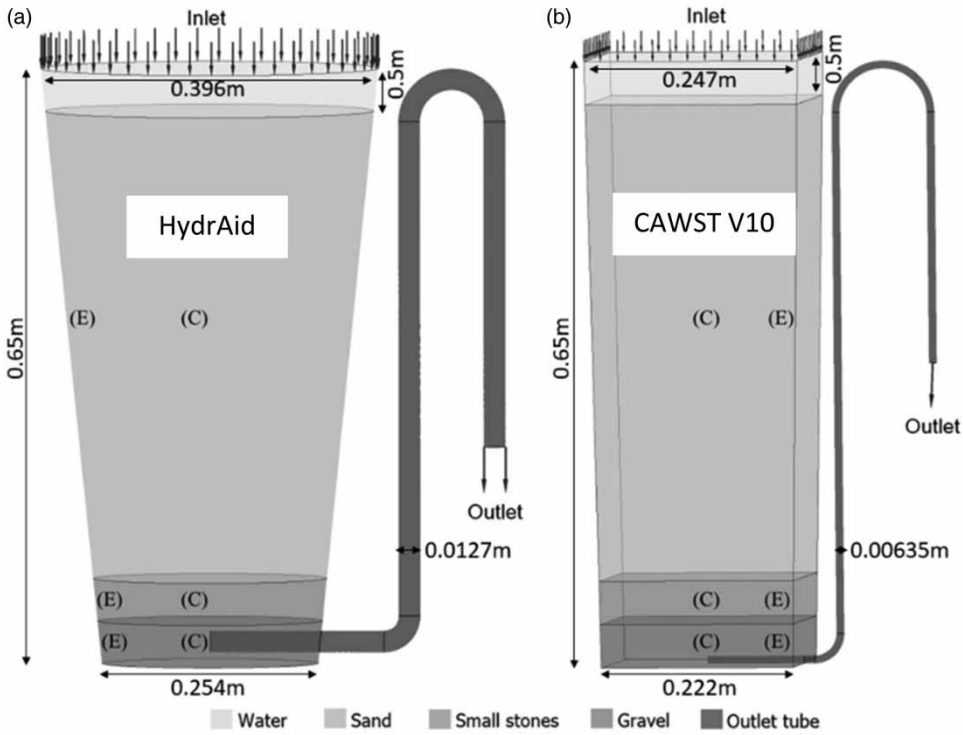

Figure 1 | Dimensions and geometry for HydrAid (a) and CAWST V10 (b). All indicated regions by (E) represent the edges of the filters for each layer, and the points (C) indicate the central region in each layer.

Table 1 | Dimensions of the HydrAid and CAWST V10 model for the evaluated depth variations (Dep)

Dimensions HydrAid (H) and CAWST V10 (CW) (m)	Dep 1 (H)	Dep 2 (H)	Dep 3 (H)	Dep 1 (CW)	Dep 2 (CW)	Dep 3 (CW)
Filter total height	0.170	1.060	1.950	0.170	1.060	1.950
Water layer height	0.030	0.100	0.150	0.030	0.100	0.150
Upper diameter	0.280	0.515	0.710	0.221	0.310	0.467
Bottom diameter	0.246	0.300	0.495	0.215	0.271	0.397

in the filter, and then, a variable inlet velocity is avoided due to numerical and computational implications. The second one has a fixed water column. Based on the previous work of Berbert *et al.* (2016), a continuous and slow feed is considered, and a water uniform velocity at *inlet condition* was fixed of 4×10^{-6} m/s.

On the *outlet condition*, its average gauge pressure was prescribed in 0.0 Pa; that is, the drainage tube is open to the atmosphere. Moreover, the reference pressure for all domains is equal to 1 atm, and for all surface walls, filter and drainage tube were fixed in the *non-slip* condition.

2.6. Porosity, permeabilities, and layer thickness

It is known that the BSF is composed of different particle layers as shown in Figure 1, and each one has a local variable porosity and permeabilities with a random distribution that may be the main factor related to the flow short-circuit; preferential pathways; and low retention times that deviates from the theoretical and original design. Nonetheless, this kind of description is computationally prohibitive and not feasible.

Under an engineering framework, a representative average value based on experimental measures and samples is more effective than a local variable porosity and permeabilities with a random distribution, this last kind of description is computationally prohibitive and not feasible.

To avoid numerical issues, a smooth transition in the physical properties of the porous domains is done next to the interfaces. Such transition is fitted by a hyperbolic tangent function:

$$k = (1 - f_1) \cdot k_{\text{sand}} + f_1 \cdot k_{\text{smallstones}} + f_2 \cdot (k_{\text{gravel}} - k_{\text{smallstones}}), \tag{8}$$

$$\varepsilon = (1 - f_1) \cdot \varepsilon_{\text{sand}} + f_1 \cdot \varepsilon_{\text{smallstones}} + f_2 \cdot (\varepsilon_{\text{gravel}} - \varepsilon_{\text{smallstones}}), \tag{9}$$

being f_1 and f_2 functions to smooth the transition between layers (Equation (10) and (11)) (Maliska *et al.* 2008):

$$f_1 = \frac{1}{2}\left[\tanh\left(\frac{h_1 - y}{\Delta}\right) + 1\right], \tag{10}$$

$$f_2 = \frac{1}{2}\left[\tanh\left(\frac{h_0 - y}{\Delta}\right) + 1\right], \tag{11}$$

where $\Delta = 0.01$ m regulates the transition thickness and should cover from 2 to 10 mesh elements. The reference heights for conventional filters were $h_0 = 0.05$ m, $h_1 = 0.10$ m, and $h_2 = 0.65$ m (total filter height).

Table 2 presents the parametric levels of the heights of layers used in the DoEs – three per layer – due to the CCD approach presented in the next section.

2.7. Design of experiments

The experimental design was carried out using the statistical method of DoEs, applying the CCD methodology, together with the RSM. For the sensitivity analysis, the statistical software STATISTICA 13.3 was implemented to qualitatively and quantitatively optimize the combinations between the analysis parameters. The first DoE model performed consisted of a combination of six independent factors, being the permeability (k) and porosity (ε) of each porous media. Each factor had three levels (Table 3) (Ashok *et al.* 2020). The values of k and ε were adopted based on the literature (Bear 1972). Besides, 4 repetitions were included, resulting in 29 cases of single executions and a total of 33 cases. The operating conditions were generated in a standard order and shown in the order of execution in Table 4.

Table 2 | Limiting heights of the inner layers of the HydrAid and CAWST V10 filters, for the three filter heights analyzed (*Dep* 1, 2, and 3)

Height (m)	Dep_1	Dep_2	Dep_3
h_0	0.02	0.08	0.15
h_1	0.04	0.16	0.30
h_2	0.17	1.06	1.95

h_2^*: filter total height.

Table 3 | Coded and actual values of formulation variables permeabilities and porosities, evaluated for the sand, small stones, and gravel layers

Factor (variable)	Coded value	Low level −1	Mid-level* 0	High level +1
k_{sand} (m^2)		1×10^{-13}	5×10^{10}	1×10^{-9}
$k_{\text{smallstones}}$ (m^2)		1×10^{-11}	5×10^{-8}	1×10^{-7}
k_{gravel} (m^2)		1×10^{-10}	5×10^{-7}	1×10^{-6}
$\varepsilon_{\text{sand}}$ (%)		20	25	30
$\varepsilon_{\text{smallstones}}$ (%)		30	35	40
$\varepsilon_{\text{gravel}}$ (%)		40	45	50

[a]Mid-level was followed for center point formulations.

Table 4 | Experimental design of CCD for different porosities and permeabilities for sand, small stones, and gravel

Cases (C)	k_{sand} (m^2)	$k_{smallstones}$ (m^2)	k_{gravel} (m^2)	ε_{sand} (%)	$\varepsilon_{smallstones}$ (%)	ε_{gravel} (%)
C1	1.00×10^{-09}	1.00×10^{-07}	1.00×10^{-06}	30	30	40
C2	1.00×10^{-09}	1.00×10^{-07}	1.00×10^{-06}	20	40	40
C3	1.00×10^{-09}	1.00×10^{-07}	1.00×10^{-10}	30	30	50
C4	1.00×10^{-09}	1.00×10^{-11}	1.00×10^{-06}	20	40	50
C5	1.00×10^{-13}	1.00×10^{-07}	1.00×10^{-10}	30	40	50
C6	1.00×10^{-09}	1.00×10^{-11}	1.00×10^{-06}	30	30	50
C7	1.00×10^{-13}	1.00×10^{-07}	1.00×10^{-06}	20	30	40
C8	1.00×10^{-09}	1.00×10^{-07}	1.00×10^{-10}	20	40	50
C9	1.00×10^{-09}	1.00×10^{-11}	1.00×10^{-10}	30	30	40
C10	1.00×10^{-13}	1.00×10^{-11}	1.00×10^{-06}	20	30	50
C11	1.00×10^{-13}	1.00×10^{-07}	1.00×10^{-10}	20	30	50
C12	1.00×10^{-09}	1.00×10^{-11}	1.00×10^{-10}	20	40	40
C13	1.00×10^{-13}	1.00×10^{-11}	1.00×10^{-10}	30	40	40
C14	1.00×10^{-13}	1.00×10^{-11}	1.00×10^{-06}	30	40	50
C15	1.00×10^{-13}	1.00×10^{-07}	1.00×10^{-06}	30	40	40
C16	1.00×10^{-13}	1.00×10^{-11}	1.00×10^{-10}	20	30	40
C17	1.00×10^{-13}	5.00×10^{-08}	5.00×10^{-07}	25	35	45
C18	1.00×10^{-09}	5.00×10^{-08}	5.00×10^{-07}	25	35	45
C19	5.00×10^{-10}	1.00×10^{-11}	5.00×10^{-07}	25	35	45
C20	5.00×10^{-10}	1.00×10^{-07}	5.00×10^{-07}	25	35	45
C21	5.00×10^{-10}	5.00×10^{-08}	1.00×10^{-10}	25	35	45
C22	5.00×10^{-10}	5.00×10^{-08}	1.50×10^{-06}	25	35	45
C23	5.00×10^{-10}	5.00×10^{-08}	5.00×10^{-07}	20	35	45
C24	5.00×10^{-10}	5.00×10^{-08}	5.00×10^{-07}	30	35	45
C25	5.00×10^{-10}	5.00×10^{-08}	5.00×10^{-07}	25	30	45
C26	5.00×10^{-10}	5.00×10^{-08}	5.00×10^{-07}	25	40	45
C27	5.00×10^{-10}	5.00×10^{-08}	5.00×10^{-07}	25	35	40
C28	5.00×10^{-10}	5.00×10^{-08}	5.00×10^{-07}	25	35	50
C29*	5.00×10^{-10}	5.00×10^{-08}	5.00×10^{-07}	25	35	45
C30*	5.00×10^{-10}	5.00×10^{-08}	5.00×10^{-07}	25	35	45
C31*	5.00×10^{-10}	5.00×10^{-08}	5.00×10^{-07}	25	35	45
C32*	5.00×10^{-10}	5.00×10^{-08}	5.00×10^{-07}	25	35	45
C33*	5.00×10^{-10}	5.00×10^{-08}	5.00×10^{-07}	25	35	45

[a]Center points are included in the design.

The second DoE model addressed two independent factors, the diameter of the outlet tube (d) and the depth of the filter bed (Dep) (Table 5). The values adopted for the outlet pipe were based on commercial PVC pipes normally found in Brazil, and the height of the filter was based on the dimensions of possible materials easily accessible to communities, for example, pipes and water tanks. Four repetitions were included, resulting in 9 single cases and a total of 13 cases. The operating conditions were generated in a standard order and shown in order of execution in Table 6.

In ANSYS CFD-Post 20.1, data of velocity and time were collected on the streamline for each case. Hydraulic retention times (HRTs) have been calculated (Cruz-Salomón *et al.* 2017). The objective was to find out for which operational configurations the velocities were lower, and the times on the streamlines and HRTs were higher. The STATISTICA 13.3 software was used to process input and response factors. The variance analysis method (ANOVA) was applied to assess the impacts of

Table 5 | Coded and actual values of formulation variable diameters of outlet tube and depth of filter bed

Factor (variable)	Coded value	Low level −1	Mid-level[a] 0	High level +1
d (m)		0.0127	0.03175	0.0508
Dep (m)		0.17	1.06	1.95

[a]Mid-level was followed for center point formulations.

Table 6 | Experimental design of CCD for different diameters of outlet tube and depth of filter bed

Cases	*d* (m)	*Dep* (m)
C1	0.012700	0.170000
C2	0.012700	1.950000
C3	0.050800	0.170000
C4	0.050800	1.950000
C5	0.012700	1.060000
C6	0.050800	1.060000
C7	0.031750	0.170000
C8	0.031750	1.950000
C9[a]	0.031750	1.060000
C10[a]	0.031750	1.060000
C11[a]	0.031750	1.060000
C12[a]	0.031750	1.060000
C13[a]	0.031750	1.060000

[a]Center points are included in the design.

variables and their possible interaction implications in the biofilter flow process (Rene *et al.* 2018). The *p*-value was assessed to determine the significance of each coefficient term. In which, $p \leq 0.05$ points to a significant variable, with a 95% confidence level (Teja & Damodharan 2018). The interaction effects established between the factors were evaluated from the response surface profiles (RSMs).

3. RESULTS AND DISCUSSION

3.1. Hydrodynamic profile for different porosities and permeabilities

The hydrodynamic behavior of HydrAid and CAWST V10 is shown in Figure 2. It is possible to separate the cases into two groups with clearly visualized similarities. The first group (group 1), represented by the profiles on the left, includes cases C1–C2, C4, C6–C7, C10, C13–C20, and C22–C33. The second model (group 2), on the right, is composed of cases C3, C5, C8–C9, C11–C12, and C21.

Comparing the two groups, the main point observed was that in group 1, the area of the edge formed with the minimum flow velocities is significantly smaller, resulting in the better use of the filter media and the total volume of the filter. When analyzing the velocity vectors as shown in Figure 2, the flow lines are similar. In case 1 (Table 4), the flow direction gradually changes to horizontal in small stones and gravel. In the second group presented, composed by case 3 of both models (Table 4), from the layer of small stones, a small region starts at the edge where the flow has minimum velocities. This condition extends to the gravel layer, forming a much larger contour than in case 1, with low flow and minimum velocities.

The results of the numerical experiments of the HydrAid and CAWST V10 models are best visualized and compared from the average velocity profiles for sand, small stones, and gravel as shown in Figure 3.

When comparing the two models, it appears that the velocity at the center of the sand layer is 1.62 times higher for HydrAid and at the edge 1.87 times higher. In the small stone layer, the center velocity is 3.45 times higher and on the edge 2.44 times

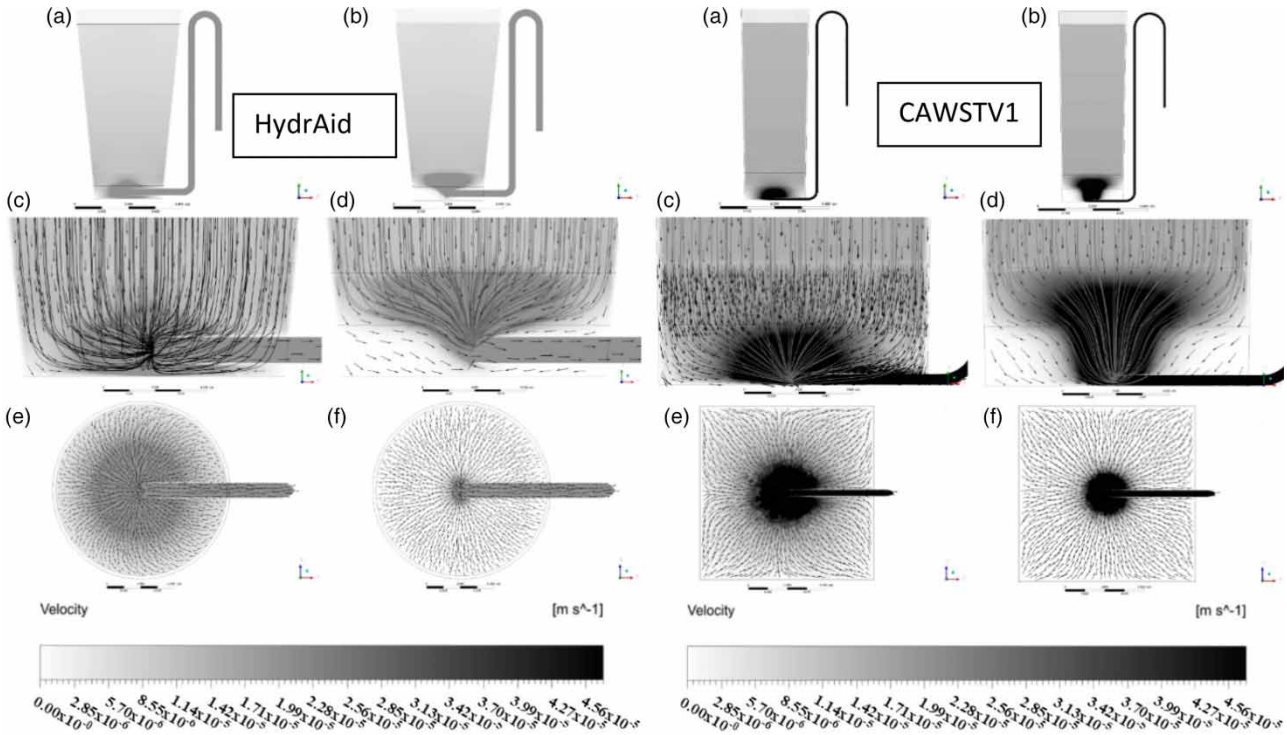

Figure 2 | Cross-section of the velocity contour (m s^{-1}) in the complete filter for cases (a) H1/CW1 and (b) H3-CW3. The transverse profile of the velocity contour (m s^{-1}), with velocity vectors, and streamlines, in the region of the outlet tube for cases (c) H1/CW1 and (d) H3/CW3. Bottom view of the filter, with velocity contour (m s^{-1}) and velocity vectors, encompassing the region of the outlet tube for cases (e) H1/CW1 and (f) H3/CW3. The color scale provides the magnitude of the velocity field, where white represents the minimum velocity and black represents the maximum velocity. The H1 case and the cases simulated for this one present a better use of the volume of a porous filter media, with higher velocities in the lower edge/base of the filter than in the H3/CW3 model. Please refer to the online version of this paper to see this figure in colour: http://dx.doi.org/10.2166/hydro.2021.087.

higher for HydrAid. These differences are explained by the difference in the diameter of the filter bed, whose top and bottom diameters of the HydrAid are much larger, and the difference in the diameter of the outlet tube. These configurations tend to favor an increase in flow velocity. On the gravel layer in the central region, the velocity in the HydrAid was 4.65 times lower than in the CAWST V10, which can be explained by the smaller diameter of the exit tube in the CAWST V10. However, the velocity at the edge of the crushed layer was 2.02 times higher in HydrAid than in CAWST V10.

The average mechanical filtration rate in sand filters is indicated as one of the most important physical factors in the treatment efficiency, considered in the range of 0.1 to 0.3 m/h or 2.78×10^{-5} to 8.3×10^{-5} m/s. The treatment process to remove contaminants occurs through biological activity in the upper layer of the filter or sand (*Schmutzdecke*) (Verma *et al.* 2017). When the filtration velocity is higher, a drag of particles can occur, preventing the maturation of the biofilm in the layer.

Based on this, the lowest velocities observed in HydrAid for the sand layer were in H1, H6, H9, and H12 (only on the edge), H13, H14, H15, and H19 (cases belonging to group 1, except H9 and H12). On CAWST V10, the cases with the lowest velocities in the sand layer were CW13, CW14, CW15, and CW24. However, considering the velocity range to favor biofilm formation (Verma *et al.* 2017), only the HydrAid filter has the most favorable velocities for treatment, as in CAWST V10, all cases presented velocities below the favorable range. Of these, more favorable cases are H7, H9, H8, H10, H11, H12, H16, H21, and H23. Very low velocities can cause problems in flow and treatment, due to excessive biofilm formation throughout the bed, that is, incrustation problems, requiring more frequent cleaning of the BSF.

In the layer of small stones in the central region of the models, the highest average velocities were observed in cases H3-CW3, H5-CW5, H8-CW8, H11-CW11, and H21-CW21. In these cases, common filter media characteristics are k_{sand} is 1.0×10^{-13} m^2, for $k_{smallstones}$ 1.0×10^{-11} or 1.0×10^{-7} m^2, and k_{gravel} 1.0×10^{-10} or 1.0×10^{-6} m^2. Also, 30% for ε_{sand}, 40% for $\varepsilon_{smallstones}$, and 40 and 50% for ε_{gravel}. In the region of the edge of the small stone layer, the lowest velocities in the two filters were observed in the same cases where the highest velocities were obtained in the central region.

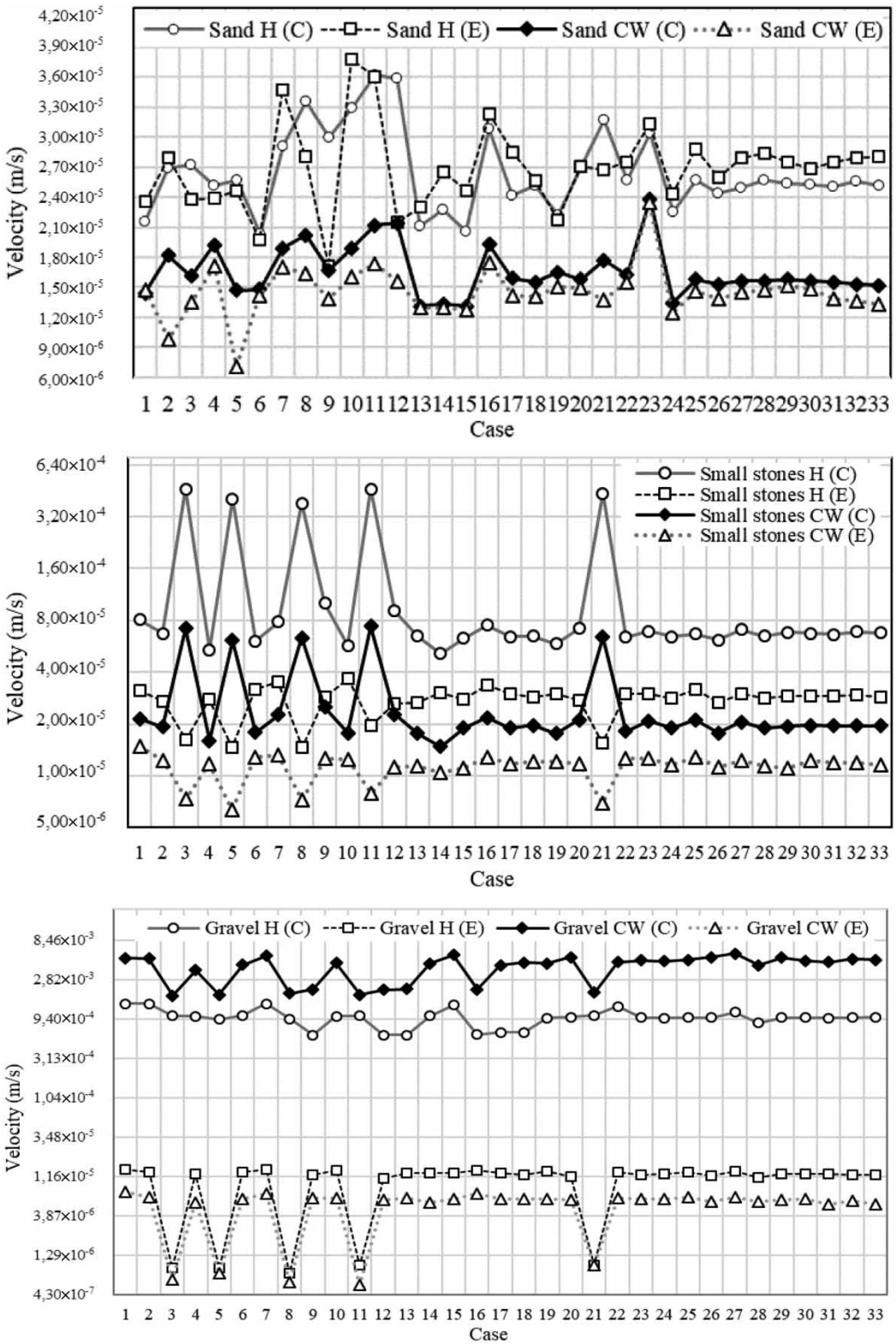

Figure 3 | Average velocities (m s^{-1}) obtained for the central region (C) and edge (E) for sand layer, small stones, and gravel in the 33 cases simulated in HydrAid (H) and CAWST V10 (CW).

In the layer of small stones in the central region of the models, the highest average velocities were observed in the cases H3-CW3, H5-CW5, H8-CW8, H11-CW11, H21-CW21. In these cases, the characteristics of the filter media in common are k_{sand} of 1.0×10^{-13} or 1.0×10^{-9} m^2, $k_{smallstones}$ of 1.0×10^{-7} m^2, k_{gravel} of 1.0×10^{-10} m^2, ε_{sand} of 20 or 30%, $\varepsilon_{smallstones}$ of 30 or 40%, and 50% ε_{gravel}. In the region of the edge of the small stone layer, the lowest velocities in the two filters were observed in the same cases in which the highest velocities were obtained in the central region.

In the HydrAid filter, in the central layer of the gravel, the lowest velocities were observed in H3, H5, H8, H9, H11, H12, H13, H16, and H21. These cases have in common a k_{sand} of 1.0×10^{-13} or 1.0×10^{-9} m^2, $k_{smallstones}$ of 1.0×10^{-11} or 1×10^{-7} m^2, k_{gravel} of 1.0×10^{-10} m^2, ε_{sand} of 20 or 30%, $\varepsilon_{smallstones}$ of 30 or 40%, and ε_{gravel} of 40 or 50%. In CAWST V10, the cases were CW9, CW12, CW13, CW16, CW17, and CW18. Here, the k_{sand} values were 1.0×10^{-13} or 1.0×10^{-9} m^2, $k_{smallstones}$ of 1.0×10^{-11} or 1.0×10^{-8} m^2, and k_{gravel} 1.0×10^{-10} or 1×10^{-7} m^2. It was not possible to verify a pattern between the porosity values for CAWST V10, requiring further statistical analysis.

In the edge region of the HydrAid and CAWST V10 filters, the highest velocities were obtained in H1-CW1, H7-CW7, H10-CW10, H16-CW16, H19-CW19, and H27-CW27. The observed pattern consists of k_{sand} of 1.0×10^{-13}, 1.0×10^{-9} or 5.0×10^{-10} m^2, combined with $k_{smallstones}$ of 1.0×10^{-11} or 1.0×10^{-7} m^2, and k_{gravel} of 1.0×10^{-6} or 5.0×10^{-7} m^2. It was not possible to predict a pattern for porosities.

In addition, the use of finer sand is another important physical factor to consider in studies on the efficiency of BSFs, as it is crucial in removing contaminants (Verma *et al.* 2017). Mulugeta *et al.* (2020) and Verma *et al.* (2017) indicate that the opening of the pores of the media in the filter, that is, the porosity, has an impact on the water flow in the filter. As the sand's porosity increases, the flow rate also increases. On the one hand, this is beneficial as it reduces the need for frequent cleaning such as backwashing. However, this causes the treatment efficiency to be reduced, by decreasing the contact time and decreasing the formation of the biofilm layer. Observing the sand porosity values in the HydrAid cases with more favorable velocities seen previously, it is obtained that the majority comprises finer sand ($\varepsilon_{sand} = 20\%$), which are then the most recommended configurations H7, H8, H10, H11, H12, H16, and H23.

In HydrAid, the longest HRTs resulted from cases H9, H12, H13, H16, H17, H18, and H28. In these cases, the predominant permeability values were k_{sand} of 1.0×10^{-13} and 1.0×10^{-9} m^2, $k_{smallstones}$ of 1.0×10^{-11} and 1.0×10^{-8} m^2, and k_{gravel} of 1.0×10^{-10} and 5×10^{-7} m^2. No porosity pattern was observed since in these cases all the porosity ranges under study are presented. However, studies show that the pore volume influences the HRT, being directly proportional to this factor, that is, the smaller the pore volume, the smaller the HRT (Freitas *et al.* 2021). According to Mulugeta *et al.* (2020), when the microorganism layer is formed, the permeability in the media decreases, consequently increasing the water retention time. This phenomenon increases the possibility of capturing suspended solids and water pathogens through mechanical entrapment, increasing treatment efficiency.

In CAWST V10, the highest HRTs were CW3, CW5, CW8, CW11, and CW21. These cases have in common a k_{sand} of 1.0×10^{-13} and 1.0×10^{-9} m^2, $k_{smallstones}$ of 1.0×10^{-7} m^2, k_{gravel} of 1×10^{-10} m^2, k_{gravel} of $1e^{-10}$ m^2, ε_{sand} of 20 or 30%, $\varepsilon_{smallstones}$ of 30 or 40%, and ε_{gravel} of 50%. The average HRT on CAWST V10 is estimated to be 77% lower than that on HydrAid. This can be explained by the reduction in the diameter of the top and bottom of the filter, as well as the diameter of the exit tube. Streamline and HRT results are available in Supplementary Material, Appendix E.

3.2. Hydrodynamic profile for different filter heights and diameters of the outlet tube

In this second part, the objective was to evaluate different diameters of the exit tube, for different heights and filter diameters. The flow velocity fields on the HydrAid and CAWST V10 filters are shown in Figure 4. The cases were grouped according to filter depth (row) and exit tube diameter (column).

When analyzing the velocity vectors, it is observed that the flow obtained vertically prevailed for a large extension of the filter, including the layer of sand and small stones. From the gravel layer, the flow direction changes to horizontal, toward the inlet of the outlet pipe. Furthermore, they indicated that the flow occurs almost through the bottom edge of the filter, with small corners where the flow is less and has minimal velocity. To compare the results, average velocity profiles were created in the central region and edge of each layer and are available in Supplementary Material, Appendix F.

The cases (C) can be separated to assess the effects of tube diameter into three groups of the same depth with different diameters, group 1 (C1, C3, and C7), group 2 (C5, C6, and C9), or group 3 (C2, C4, and C8). The groups were separated to compare the effects of depth, in the same diameter with different depths, group 4 (C1, C5, and C2), group 5 (C3, C6, and C4), and group 6 (C7, C9, and C8). When analyzing the cases of the two filters in the gravel layer (central), it is observed

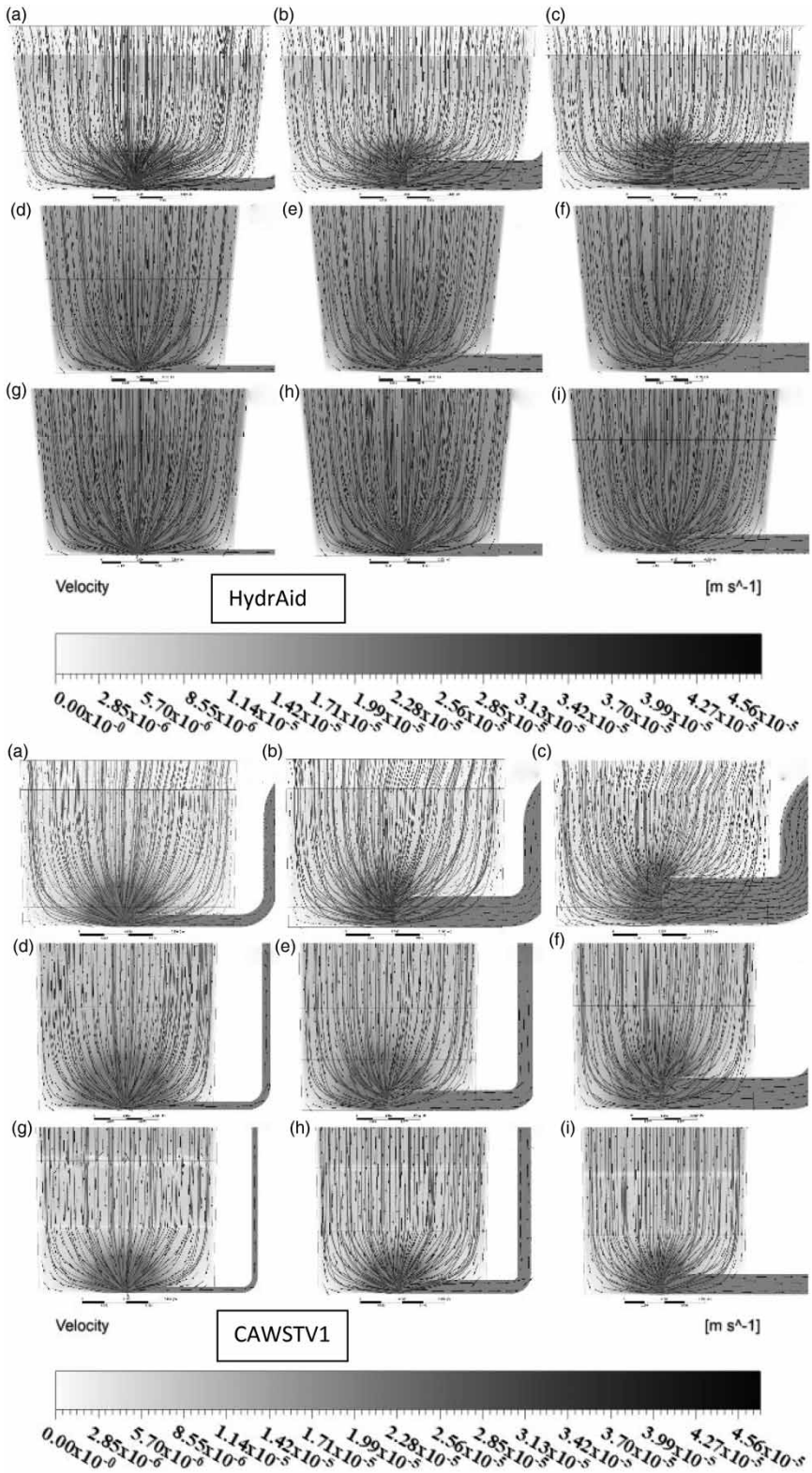

Figure 4 | Cross-section of the velocity contour (m s^{-1}), with velocity vectors, and streamlines, in the region of the outlet tube for the cases evaluated in the HydrAid and CAWST model. (a) case 1 ($Dep_1 \times d_1$), (b) case 7 ($Dep_1 \times d_2$), (c) case 3 ($Dep_1 \times d_3$), (d) case 5 ($Dep_2 \times d_1$), (e) case 9 to 13 ($Dep_2 \times d_2$), (f) case 6 ($Dep_2 \times d_3$), (g) case 2 ($Dep_3 \times d_1$), (h) case 8 ($Dep_3 \times d_2$), and (i) case 4 ($Dep_3 \times d_3$). The color scale in the sidebar establishes the magnitude of the velocity field, where white represents the lowest velocity (minimum) and black represents the highest velocity (maximum). Please refer to the online version of this paper to see this figure in colour: http://dx.doi.org/10.2166/hydro.2021.087.

that the smaller the diameter, the greater the velocity. For the same diameters, velocity increases with increasing height. In cases with Dep_1 in the gravel layer (edge), the larger the diameter (d_3), the greater the velocity.

The difference observed between the models was that for Dep_1 of HydrAid, d_2 implies greater velocity in the region, followed by $d3$. At the other depths of both filters, for Dep_2, the highest velocity was obtained with d_2, followed by d_3. In Dep_3, the highest velocities were obtained with d_3, followed by d_2. Also, the streamline times on HydrAid are longer than those on CAWST V10. The longest times were obtained in the highest filters. Besides, it was obtained that for larger diameters, the time was greater. The average flow time for CAWST V10 is 1.2 times less than that for HydrAid (for Dep_1 height). In Dep_2, the time in CAWST V10 is 1.4 times shorter, and in Dep_3, it is 2.1 times shorter.

When evaluating the velocity range to favor biofilm formation (Verma *et al.* 2017), again at this stage of the study, only the HydrAid filter has the most favorable velocities for treatment, as in CAWST V10, all cases presented velocities below from the favorable range. The most favorable cases and, therefore, indicated as the basis for choosing the operating parameters are H1, H2, H4, and H8, that is, the entire group 3 (C2, C4, and C8) and C1 of group 1; therefore, the greater depth of the bed (Dep_3) favors the operation and treatment in BSFs.

The highest HRTs were obtained in C4 ($Dep_3 \times d_3$) and C8 ($Dep_3 \times d_2$) in CAWST V10, composed of cases with Dep_3, d_2, and d_3. In HydrAid, there were C3 ($Dep_1 \times d_3$), C4 ($Dep_3 \times d_3$), and C6 ($Dep_2 \times d_3$), thus being the d_3 factor with the greatest impact. However, a larger diameter allows for higher HRTs. In general, the average HRT in HydrAid is 1.6 times less than CAWST V10 for Dep_1, 2.6 times less for Dep_2, and 7.7 times less for Dep_3. This can be explained by the difference in the diameter of the filters since the diameters of the HydrAid model are larger than the diameters of the CAWST V10. With a narrower duct, the flow requires less flow time than in a larger duct. Furthermore, higher HRTs were observed in filters with greater bed depth in both filters, and vice versa. This condition was also observed in the study by Freitas *et al.* (2021).

3.3. Statistical analysis

Important factors that can impact water treatment are HRT and velocities in the sand and on the gravel edge. Therefore, only these were analyzed with the ANOVA tables (Supplementary Material, Appendices D and E). As the velocity in the edge region in the sand layer did not differ considerably from the central region, only the central one was studied.

3.3.1. HRT

Evaluating the first experimental part in HydrAid, it was observed with the values of p and F, that the factors with the greatest impact on HRT were the permeability and porosity of the gravel layer. The regression model was adopted to formulate the response surfaces of the most significant interaction on the HRT variable, which was $kG * \varepsilon G$ (Figure 5(a)). There are two possibilities to obtain the highest HRTs. An independent kG can be applied in a range of 1×10^{-7} to $1. \times 10^{-6}$ m^2 for εG between 38 and 45%. Another possibility is a kG between 5×10^{-7} and 1.2×10^{-6} m^2 for independent εG in the range of 38 to 52%.

In CAWST V10, the factor with the greatest significant linear effect on HRT was gravel permeability (kG). Evaluating the interactive effects, the only ones that reached a degree of significance were the $\varepsilon S * \varepsilon SS$ (Figure 5(b)). It is observed in the RSM of the $\varepsilon SS * \varepsilon S$ interaction that the highest HRTs were obtained in borderline values. For this purpose, high HRTs are found in εSS (39–42 or 28–31%) for εS (18–21%) or εSS (39–42 or 28–31%) for εS (27–32%).

The results of the second experimental part were studied. In the HydrAid filter, both the diameter of the tube (d) and the depth of the filter (Dep) were significant in the variation of time. Investigating the values of F, p, and MS, it can be determined, however, that the diameter has a greater impact. The $d * Dep$ interaction was not significant in this filter. In CAWST V10, ANOVA showed significance in d, Dep, and in the interaction $d * Dep$. It was possible to infer that the diameter of the tube has a much greater impact on HRT than the other factors, as well as HydrAid. The profile of the response surface of the $d * Dep$ interaction is shown in Figure 5(c). It can be seen that the larger the diameter of the tube and the greater the depth of the filter, the greater the HRT. The highest HRTs were obtained with $d \geq 0.030$ and $Dep \geq 1.2$.

3.3.2. Velocity in the sand (center)

In HydrAid, the factor that most influences sand velocity was sand porosity, followed by gravel permeability. The most significant interaction effects were $kS * \varepsilon G$ and $kG * \varepsilon S$. From the response surfaces of the most significant interactions (available in Supplementary Material, Appendix G), it is observed that to establish lower velocities in this layer, there are two possibilities of combinations. The first is to combine kG in the range of 6×10^{-7} to 1.2×10^{-6} m^2 with an independent

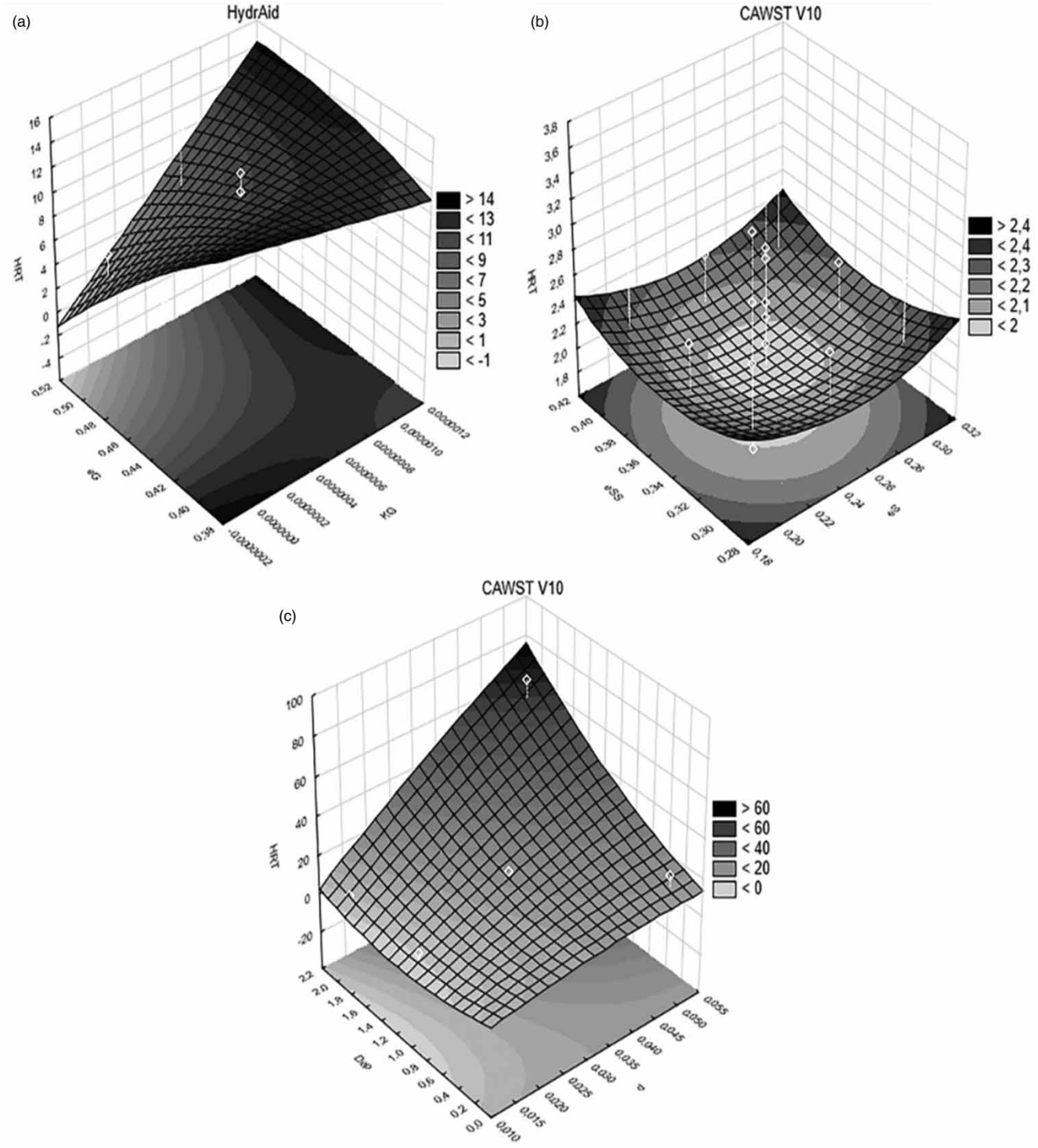

Figure 5 | RSM for the HRT variable (a) εG vs. kG in HydrAid, (b) εS vs. εSS in CAWST V10, and (c) d vs. Dep in the CAWST V10.

kS in the range of 1×10^{-7} to 5×10^{-7} m^2. The second consists in combining a kS between 1×10^{-10} and 1.2×10^{-9} m^2, with εG between 38 and 44%.

In the CAWST V10 model, the most significant factor was εS for the linear effect. Among the interactive effects, significance was obtained for $\varepsilon SS * kS$. In this interaction (available in appendix G), it is possible to verify that the velocity is lower when the εSS is 28% or is in the range of 39% to 42%, for an independent kS between 1.0×10^{-10} and 1.2×10^{-9} m^2.

Table 7 | Recommendations of configurations for better hydrodynamics in HydrAid and CAWST V10, to obtain better results in water treatment.

Measured parameter	Recommendation for HydrAid	Recommendation for CAWST V10
HRT	kG (1.0×10^{-7}-1.2×10^{-6} m^2) and εG (38-45%); kG (5.0×10^{-7}-1.2×10^{-6} m^2) and εG (38-52%);	εSS (39-42% or 28-31%) and εS (18-21%); εSS(39-42% or 28-31%) and εS (27-32%); $d \geq 0.030$ and$Dep \geq 1.2$;
Velocity sand (C)	kG (6.0×10^{-7}-1.2×10^{-6} m^2) and kS (1×10^{-7}-5×10^{-7} m^2); kS (1.0×10^{-10}-1.2×10^{-9} m^2) and εG (38-44%); d (0.010-0.030 m) and Dep (0.0-2.2 m); d(0.010-0.055 m) and Dep (0.4-2.2 m);	eSS (28% or 39%-42%) and kS (1×10^{-10}-1.2×10^{-9} m^2); d (0.010-0.030 m) and Dep (0-2.2 m); d(0.010-0.055) and Dep (0.4-2.2 m);
Velocity gravel (E)	kG (5.0×10^{-7}-1.2×10^{-6} m^2) and kSS (1.0×10^{-8}-1.2×10^{-7} m^2).	kSS (1.0×10^{-8}-1.2×10^{-7} m^2) and kG (5.0×10^{-7}-1.2×10^{-6} m^2); kG (1×10^{-8}-4×10^{-8}) and εG (38-44%); kSS (1.0×10^{-7}-1.2×10^{-7}) and εG (49-52%); kG (1.0×10^{-7}-1.2×10^{-6} m^2) and εG (38-43%); kG (7.0×10^{-7}-1.2×10^{-6} m^2) and εG (38-52%); d (0.010-0.055 m) and Dep (0.4-2.2 m).

In the second experimental part of HydrAid, the factor that mostly impacts the velocity of the layer is d. However, Dep and $d * Dep$ also have some influence. In CAWST V10, Dep had a greater effect on velocity than d, and the interaction of both implies a greater impact than the factors separately. In both the RSMs (available in Supplementary Material, Appendix G) to establish lower velocities in the central region of the sand, the diameter must be from 0.010 to 0.030 m for independent Dep (0.0–2.2 m). Another possibility is the adoption of an independent d (0.010–0.055 m) for Dep between 0.4 and 2.2 m.

3.3.3. Velocity in the gravel (edge)

For velocity parameter in the gravel layer for the edge of the HydrAid filter, ANOVA showed greater significance for kG, and $kSS * kG$. It is observed that for higher velocities kG, values between 5.0×10^{-7} to 1.2×10^{-6} m^2 must be adopted. Combined with this, the can be independent in the range of 1.0×10^{-8} to 1.2×10^{-7} m^2.

The factors that had the most significant effect on CAWST V10 were kG, $kSS * kG$, $kSS * \varepsilon G$, and $kG * \varepsilon G$. In the interaction $kSS * kG$, the kSS can be from 1.0×10^{-8} to 1.2×10^{-7} m^2, and the higher the kG (5×10^{-7} to 1.2×10^{-6} m^2), the greater the velocity. In the $kSS * kG$ interaction, two combinations with high velocities are obtained. One comprises $1.0 \times 10^{-8} \leq kG \leq 4 \times 10^{-8}$ and $0.38 \leq \varepsilon G \leq 0.44$, and the other, $1.0 \times 10^{-7} \leq kSS \leq 1.2 \times 10^{-7}$ and $0.49 \leq \varepsilon G \leq 0.52$. In the latter, $kG * \varepsilon G$, higher velocities are observed when εG is in the range of 38 to 43% kG for from 1.0×10^{-7} to 1.2×10^{-6} m^2, or when kG is in range of 7.0×10^{-7} to 1.2×10^{-6} m^2, and εG by 38 to 52%.

Still, at HydrAid, it was found that the factor that had the greatest impact on velocity was depth. The $Dep * d$ interaction was not significant for this filter. In CAWST V10, the greatest significance was also in Dep. Also, the $d * Dep$ interaction was significant. The highest velocities can be obtained for Dep between 0.4 and 2.2 m, and d in the range 0.010–0.055 m (results are available in Supplementary Material, Appendix G).

3.4. Recommendations for BSF projects

The best physical conditions were studied to provide lower velocities, mainly in the sand layer, where a large part of the biofilm develops, and in the gravel layer (edge), where lower velocity zones and slower flow occur. A summary of the results is shown in Table 7. Given the results obtained, it is possible to state that in terms of geometry, the CAWST V10 model presents better hydrodynamics for water treatments due to the observed lower velocities and longer time in the streamline. HRTs are also higher in CAWST V10, being favorable to the maturation of the biofilter.

4. CONCLUSIONS

BSFs are one of the water treatment technologies at the POU installed in areas where drinking water is not available or is limited. Besides, it is generally distributed by nonprofit organizations around the world, as well as being easily constructed by the population residing in these communities. Due to its great social and health importance, detailed studies are necessary

to understand the hydrodynamic parameters involved, enabling improvements in the process. In this study, different filter geometries, porosity, and permeability of the layers of the filter media, diameters of the outlet tube, in addition to heights, and diameters of the filters were evaluated.

The models proved to be numerically stable and capable of predicting the distribution of water in the BSFs. In general, the CAWST V10 model presented more favorable hydrodynamic conditions than HydrAid, due to its lower velocities along the entire length of the filter bed, higher HRTs, and longer times in the streamline. These factors favor microbiological growth and consequent water treatment. The best internal porosity and permeability configurations were presented for better hydrodynamics. When evaluating different heights and diameters of filters, and different diameters of pipes, it was observed that it is possible to apply this water treatment technology both on a small scale, for a residence, for example, and on a large scale, for a community.

ACKNOWLEDGEMENTS

The authors thank CAPES (Coordination for the Improvement of Higher Education) and the Araucaria Foundation (88887.350033/2019-00-CP 11/2018) for the Support of Scientific and Technological Development of Paraná for the support given to carry out this study.

DATA AVAILABILITY STATEMENT

All relevant data are included in the paper or its Supplementary Information.

REFERENCES

Ait-Mouheb, N., Schillings, J., Al-Muhammad, J., Bendoula, R., Tomas, S., Amielh, M. & Anselmet, F. 2019 Impact of hydrodynamics on clay particle deposition and biofilm development in a labyrinth-channel dripper. *Irrig. Sci.* **37**, 1–10. https://doi.org/10.1007/s00271-018-0595-7.

Almeida, R. A., Rezende, R. V. P., Mataczinski, A. K., Khan, A. I., Camilo, R., Ravagnani, M. A. S. S. & Lautenschlager, S. R. 2020 Three-dimensional simulation of a secondary circular settling tank: flow pattern and sedimentation process. *Braz. J. Chem. Eng.* **37**, 333–350. https://doi.org/10.1007/s43153-020-00030-0.

ANSYS 2020 *CFX Manual Versão 20.1*. ANSYS, Waterloo, Canadá.

Ashok, B., Jeevanantham, A. K., Bhat Hire, K. R., Kashyap, V. & Saiteja, P. 2020 Calibration of idling characteristics for lemon peel oil using central composite design in light commercial vehicle diesel engine. *Energy Convers. Manage.* **221**, 113183. https://doi.org/10.1016/j.enconman.2020.113183.

Bagheri, M. & Mohseni, M. 2014 Computational fluid dynamics (CFD) modeling of VUV/UV photoreactors for water treatment. *Chem. Eng. J.* **256**, 51–60. https://doi.org/10.1016/j.cej.2014.06.068.

Bear, J. 1972 *Dynamics of Fluids in Porous Media*, 1st edn. American Elsevier, New York.

Berbert, A. C., Almeida, R., Rezende, R. V. d. P. & Lautenschlager, S. 2016 Uso de cfd para análise de coleta de água em um filtro de bioareia com alimentação contínua. In: *XXI Congresso Brasileiro de Engenharia Química*. pp. 1–9. https://doi.org/10.13140/RG.2.2.30261.27366.

Carpenter, C. M. G. & Helbling, D. E. 2017 Removal of micropollutants in biofilters: hydrodynamic effects on biofilm assembly and functioning. *Water Res.* **120**, 211–221. https://doi.org/10.1016/j.watres.2017.04.071.

Chan, N., Young-rojanschi, C. & Li, S. 2018 Effect of water-to-cement ratio and curing method on the strength, shrinkage and slump of the biosand filter concrete body. *Water Sci. Technol.* **77**, 1744–1750. https://doi.org/10.2166/wst.2018.063.

Chawla, C., Zwijnenburg, A., Kemperman, A. J. B. & Nijmeijer, K. 2017 Fouling in gravity driven point-of-use drinking water treatment systems. *Chem. Eng. J.* **319**, 89–97. https://doi.org/10.1016/j.cej.2017.02.120.

Chen, Y., Xie, L., Cai, W. & Wu, J. 2019 Pilot-scale study using biotrickling filter to remove H2S from sewage lift station: experiment and CFD simulation. *Biochem. Eng. J.* **144**, 177–184. https://doi.org/10.1016/j.bej.2019.02.003.

Cruz-Salomón, A., Ríos-Valdovinos, E., Pola-Albores, F., Lagunas-Rivera, S., Meza-Gordillo, R. & Ruíz-Valdiviezo, V. M. 2017 Evaluation of hydraulic retention time on treatment of coffee processing wastewater (CPWW) in EGSB bioreactor. *Sustainability* **10**. https://doi.org/10.3390/su10010083.

Freitas, B. L. S., Terin, U. C., Fava, N. d. M. N. & Sabogal-Paz, L. P. 2021 Filter media depth and its effect on the efficiency of household slow sand filter in continuous flow. *J. Environ. Manage.* **288**. https://doi.org/10.1016/j.jenvman.2021.112412.

Hojo, L. Y. C. P., Rezende, R. V. d. P., Lautenschlager, S. R. & Sabogal-Paz, L. P. 2022 Household slow sand filters operating in continuous and intermittent flows: computational fluid dynamics simulation and validation by tracer experiments. *Chem. Eng. Sci.* **247**, 117058. https://doi.org/10.1016/j.ces.2021.117058.

Karpinska, A. M., Dias, M. M., Boaventura, R. A. R. & Santos, R. J. 2015 Modeling of the hydrodynamics and energy expenditure of oxidation ditch aerated with hydrojets using CFD codes. *Water Qual. Res. J. Canada* **50**, 83–94. https://doi.org/10.2166/wqrjc.2014.036.

Kennedy, T. J., Hernandez, E. A., Morse, A. N. & Anderson, T. A. 2012 Hydraulic loading rate effect on removal rates in a biosand filter: a pilot study of three conditions. *Water Air Soil Pollut.* **223**, 4527–4537. https://doi.org/10.1007/s11270-012-1215-4.

Maliska, C. R., Silva, A. F. C., Rezende, R. V. P. & Georg, I. C. 2008 Interface forces calculation for multiphase flow simulation. In *1° Encontro Brasileiro Sobre Ebulição, Condensação e Escoamento Multifásico Líquido-Gás*. pp. 1–10.

Martínez, J., Piscaglia, F., Montorfano, A., Onorati, A. & Aithal, S. M. 2017 Influence of momentum interpolation methods on the accuracy and convergence of pressure–velocity coupling algorithms in OpenFOAM®. *J. Comput. Appl. Math.* **309**, 654–673. https://doi.org/10.1016/j.cam.2016.03.037.

Mesquita, M., Testezlaf, R. & Ramirez, J. C. S. 2012 The effect of media bed characteristics and internal auxiliary elements on sand filter head loss. *Agric. Water Manag.* **115**, 178–185. https://doi.org/10.1016/j.agwat.2012.09.003.

Mulugeta, S., Helmreich, B., Drewes, J. E. & Nigussie, A. 2020 Consequences of fluctuating depth of filter media on coliform removal performance and effluent reuse opportunities of a bio-sand filter in municipal wastewater treatment. *J. Environ. Chem. Eng.* **8**. https://doi.org/10.1016/j.jece.2020.104135.

Nørregaard, A., Bach, C., Krühne, U., Borgbjerg, U. & Gernaey, K. V. 2019 Hypothesis-driven compartment model for stirred bioreactors utilizing computational fluid dynamics and multiple pH sensors. *Chem. Eng. J.* **356**, 161–169. https://doi.org/10.1016/j.cej.2018.08.191.

Qi, W.-K., Guo, Y.-L., Xue, M. & Li, Y.-Y. 2013 Hydraulic analysis of an upflow sand filter: tracer experiments, mathematical model and CFD computation. *Chem. Eng. Sci.* **104**, 460–472. https://doi.org/10.1016/j.ces.2013.09.035.

Rene, E. R., Sergienko, N., Goswami, T., López, M. E., Kumar, G., Saratale, G. D., Venkatachalam, P., Pakshirajan, K. & Swaminathan, T. 2018 Effects of concentration and gas flow rate on the removal of gas-phase toluene and xylene mixture in a compost biofilter. *Bioresour. Technol.* **248**, 28–35. https://doi.org/10.1016/j.biortech.2017.08.029.

Rezende, R. V. P., Soares, C., Bagnariolli, B., Koepp, J. & Porto, L. M. 2010 Modeling and simulation of macromolecule delivering into a rat spinal cord. In *The 6th Latin American Congress of Artificial Organs and Biomaterials*. pp. 1–16.

Singer, S., Skinner, B. & Cantwell, R. E. 2017 Impact of surface maintenance on BioSand filter performance and flow. *J. Water Health* **15**, 262–272. https://doi.org/10.2166/wh.2017.129.

Sizirici, B. 2018 Modified biosand filter coupled with a solar water pasteurizer: Decontamination study. *J. Water Process Eng.* **23**, 277–284. https://doi.org/10.1016/j.jwpe.2018.04.008.

Teja, S. P. S. & Damodharan, N. 2018 23 full factorial model for particle size optimization of methotrexate loaded chitosan nanocarriers: a design of experiments (DoE) approach. *Biomed Res. Int.* **2018**. https://doi.org/10.1155/2018/7834159.

Verma, S., Daverey, A. & Sharma, A. 2017 Slow sand filtration for water and wastewater treatment – a review. *Environ. Technol. Rev.* **6**, 47–58. https://doi.org/10.1080/21622515.2016.1278278.

Vilà-rovira, A., Ruscalleda, M., Balaguer, M. D. & Colprim, J. 2017 Hydrodynamic simulations and biological modelling of an Anammox reactor. *J. Chem. Technol. Biotechnol* 1–8. https://doi.org/10.1002/jctb.5480.

First received 19 June 2021; accepted in revised form 15 December 2021. Available online 31 December 2021